Initial Corrosion Behaviors of Fe20Cr25NiNb Stainless Steel in High Temperature Environment with Different Relative Humidity Values

HONGSHENG CHEN [1,3] HAIBO WANG,[2] QINGZHU SUN,[2]
JIANCHAO HE,[1] and XUESONG LENG[1,4]

1.—Institute of Special Environments Physical Sciences, Harbin Institute of Technology (Shenzhen), Shenzhen 518055, China. 2.—College of Vanadium and Titanium, Panzhihua University, Panzhihua 617000, China. 3.—e-mail: chenhongsheng@hit.edu.cn. 4.—e-mail: lengxuesong@hit.edu.cn

The initial corrosion behaviors of Fe20Cr25NiNb austenitic stainless steel are investigated at 1000°C in helium environment with different relative humidity values. Results show that thin chromia film and small nodules are formed for all oxidation conditions, and some white-colored large nodules are developed for the conditions with ≥ 20% relative humidity. The number and size of these large nodules increase slightly with the increase of relative humidity. These small nodules are primarily composed of the pre-formed chromia film and new-generated chromia phases, and their formation is strongly related to the oxidation of intergranular Fe_2Nb phases. The white-colored large nodules mainly consist of three oxide layers: outer magnetite layer, inner spinel layer and (Cr, O)-rich healing layer. An accelerated oxidation is observed after the transition point for the conditions with ≥ 20% relative humidity, which is attributed to the formation of large nodules. The oxide growth primarily follows the linear law before the transition point and obeys the parabolic law after the transition point for higher relative humidity.

INTRODUCTION

Advanced gas-cooled reactor is an improved Generation II gas-cooled reactor in UK, which primarily originates from one of Generation I gas-cooled reactors, namely the Magnox reactor.[1] The advanced gas-cooled reactors use graphite as the neutron moderator and carbon dioxide as coolant. The carbon dioxide coolant usually contains some additions, such as carbon monoxide, methane, water vapor, hydrogen and other minor constituents.[2] During the operation at high temperatures, the coolants with oxidation and carbonization components inevitably possess an important influence on the microstructure and service performance of the in-pile materials in the advanced gas-cooled reactors. Therefore, a lot of work has been carried out to investigate the oxidation behaviors and properties of structural steels and alloys for the advanced gas-cooled reactors in the past.[1–7]

Fuel cladding is one of crucial materials in the advanced nuclear reactors, which plays a role in preventing the release of radioactive fission products from the fuel pellets into the primary circuit and external environment.[8] The fuel cladding must be robust enough to prevent fission gas release and to ensure the nuclear safety for the advanced gas-cooled reactors.[9] Compared with other structural materials, the service conditions of fuel cladding are almost the most severe because they are in direct contact with nuclear fuels and experience extreme irradiance dose and high service temperature. For the radiation dose, the fuel cladding not only withstands the highest neutron flux among the structural materials, but also experiences intense radiation damage induced by the recoil fission fragments.[10] For the service temperature, the peak channel outlet temperature of carbon dioxide

coolant is about 661°C and the maximum temperature of fuel cladding is > 700°C.[11,12] Consequently, the oxidation behaviors and radiation resistance of fuel cladding at high temperatures are important factors that determine the service life of fuel elements and the safety of the reactor system.

In general, Fe20Cr25NiNb austenitic stainless steel has acceptable oxidation resistance in carbon dioxide, superior high-temperature compatibility with fuel pellets and good structural stability in the moderate temperatures, and therefore this steel is currently being used as the fuel cladding in advanced gas-cooled reactors.[13,14] many experiments have been performed to evaluate the service behaviors of Fe20Cr25NiNb austenitic stainless steel at the temperature range of 500–850°C.[14–21] Many researchers focused on the oxidation behaviors of Fe20Cr25NiNb stainless steel in carbon dioxide at high temperatures. Tyler et al.[14] investigated the oxidation of Fe20Cr25NiNb stainless steel in carbon dioxide at 700°C and revealed that chromium oxides were first formed on the steel surface and then transformed into the spinel oxides with the extension of oxidation time. However, at higher temperature of 800°C, the oxides first formed on the Fe20Cr25NiNb stainless steel were spinel oxides, which were rich in Fe with some quantities of Cr and Mn.[18] Usually, a Cr-rich oxide layer could be preferentially formed on the Fe20Cr25NiNb stainless steel, and the growth of oxide layer was controlled by the diffusion of Cr atom across the oxide layer at the first oxidation stage.[19] These Cr-rich oxides might be subjected to rupture as a result of the large thermal stresses or growth stresses during the growth process and resulting in the formation of spinel oxides and magnetite oxide.[13] When the Cr concentration is below a critical value in the Cr-depleted matrix of stainless steel, the Cr-rich healing layer could not be rapidly formed on the steel surface after the rupture of Cr-rich oxides, resulting in the formation of Fe-rich and Ni-rich oxides.[20,21]

Therefore, the initial corrosion behaviors of Fe20Cr25NiNb stainless steel, especially involving the transition process of oxide layer from Cr-rich oxides into Fe-rich and Ni-rich oxides, are very important for understanding the oxidation behaviors at high temperatures. On the other hand, under extreme conditions or accident conditions, the temperature of cladding steel in advanced gas-cooled reactors may quickly reach 1000°C or even higher.[13] However, there are only a few studies investigating the corrosion behaviors of Fe20Cr25NiNb stainless steel at higher temperatures (≥ 1000°C). Recently, Chen et al.[13] performed the oxidation experiment of Fe20Cr25NiNb stainless steel in an oxidizing environment at 1000°C and found the transition process of oxide layer at exposure time of about 1.5 h, but the influence of oxygen content (such as relative humidity, oxygen partial pressure or others) on the

initial corrosion behaviors of Fe20Cr25NiNb stainless steel at higher temperature is still unclear at present. In this study, the initial corrosion behaviors of the Fe20Cr25NiNb stainless steel with different relative humidity values will be investigated in isothermal helium environment at 1000°C, and the influence of relative humidity on the initial corrosion behaviors will be emphatically discussed in the present study.

EXPERIMENTAL PROCEDURE

The Fe20Cr25NiNb austenitic stainless steel was supplied by University of Science & Technology Beijing. This steel was produced by the method of vacuum induction melting and directional solidification, followed by rolling and solution treatment. For the corrosion testing, square specimens with a size of 10 mm × 10 mm × 1 mm were cut from the steel plates by the electro-spark machining method. A hole with diameter of 2 mm was drilled near one end of the specimens for hanging the testing specimens during the high-temperature corrosion. Before the corrosion experiments, the surfaces of corrosion specimens were mechanically ground up to 1000 grit SiC papers, followed by ultrasonically cleaning in acetone for 5 min and drying by drier.

The corrosion experiments were performed in the simultaneous TGA&DTA/DSC thermal analyzer (Setsys Evo, Setaram). In each individual experiment, a specimen was hung on a platinum wire and then slowly dropped into the reaction furnace of the simultaneous thermal analyzer. To remove the residual air, pure helium with 99.999% purity was first introduced into the thermal analyzer system before heating up the furnace. Then, the pure helium was introduced into a controlled humidity generator (Wetsys, Setaram) with flow rate of 20 ml/min. Subsequently, the helium gas carried trace amounts of water vapor into the reaction furnace of thermal analyzer. The pressure of helium gases with small amount of water vapor was always maintained at one atmosphere in the humidity generator and thermal analyzer. The amounts of water vapor were controlled by setting the relative humidity at the temperature of 50°C in the humidity generator before the helium gases were introduced into the reaction furnace of thermal analyzer.

During the corrosion testing, the specimens were slowly heated to 1000°C with heating rate of 10°C/min. The isothermal corrosion tests were conducted at 1000°C for 4 h. During the entire corrosion process, the temperature, relative humidity and weight change of corrosion specimens were monitored in real time by the simultaneous thermal analyzer and the photoelectric microbalance with a high gravimetric resolution of 0.02 μg. In different corrosion tests, the relative humidity was maintained at 0%, 20%, 40%, 60% and 80%, respectively. The recorded relative humidity data had higher stability and accuracy (± 0.2% RH) for all corrosion

tests, as shown in Fig. S1 (refer to online supplementary material). When the isothermal corrosion tests were finished, the corrosion specimens were cooled down with cooling rate of 10°C/min. After the corrosion experiments, the microstructure and chemical distributions of the oxidized specimens were examined by an FEI NOVA NanoSEM400 scanning electronic microscope (SEM) equipped with an Oxford energy-dispersive spectrometer (EDS). In addition, the microstructure and phases of the un-oxidized specimens were also examined by SEM and JEOL JEM-2100 transmission electron microscopy (TEM). Based on the SEM and TEM images, a dimensional measurement software (Mias, developed by Sichuan University) was used to measure the grain size of austenitic stainless steel and the size of the second phases. The oxide phases were examined by PANalytical X'pert Pro MPD x-ray diffraction (XRD) in the 2θ range of 20°–100° with a diffraction rate of 5°/min.

RESULTS AND DISCUSSION

Characterization of the Un-oxidized Fe20Cr25NiNb Stainless Steel

The chemical composition of the as-received Fe20Cr25NiNb austenitic stainless steel was analyzed by inductively coupled plasma mass spectroscopy, and the results are presented in Table S1 (refer to online supplementary material). This chemical composition is very similar with 310S stainless steel with more Ni content and less Cr content. In fact, the Fe20Cr25NiNb stainless steel is developed on the basis of 310 stainless steel.[22] The purpose of reducing Cr content is to mitigate the precipitation of brittle σ phases and increasing Ni content to improve the toughness of stainless steel. Moreover, it also can be found that the Fe20Cr25-NiNb stainless steel contains higher Mo content and a certain amount of Nb. Mo is added to improve the high-temperature strength and creep resistance, while Nb is added to enhance the strength by forming the niobium carbides with free carbon and to increase the sensitization resistance of austenitic stainless steels. In general, austenitic stainless steels are vulnerable to the intergranular corrosion at the temperature range of 420–850°C, because the Cr-depletion regions in the matrix are easily formed near the grain boundaries as a result of the precipitation of chromium carbides at the grain boundaries.[23] Nb can serve as a stabilizer to capture free carbon and to relieve the formation of Cr-depleted regions.[14]

Figure 1a shows the SEM microstructure of the un-oxidized Fe20Cr25NiNb stainless steel. The grain size of austenitic stainless steel is $\sim 25.0 \pm 4.6$ μm, and some annealing twins are observed in the grains of stainless steel, indicating that this stainless steel has relatively lower stacking fault energy and twin boundary energy. More importantly, a large amount of second phases with submicron size is observed adjacent to the grain boundaries, as indicated by the white arrows in Fig. 1a. Further TEM micrograph reveals that these second phases are entirely localized at the grain boundaries, as shown in Fig. 1b. The size of these second phases is $\sim 146 \pm 28$ nm, measured by the dimensional measurement software (Mias). The EDS results in Fig. 1d illustrate that the intergranular phases are rich in Fe and Nb. Combined with the selected area electron diffraction pattern of the intergranular phases shown in Fig. 1c, it can be confirmed that these intergranular second phases are Fe_2Nb Laves phases. This result is in accordance with the description of Refs. 24, and 25 which pointed out that the Fe_2Nb Laves phases were preferentially precipitated at the grain boundaries in the many Nb-bearing stainless steels. These intergranular Fe_2Nb Laves phases may act as free carbon traps to form the niobium carbides during the corrosion in high-temperature carbon dioxide environment.[14]

Microstructure of the Oxidized Fe20Cr25NiNb Stainless Steel

Figure 2 shows the surface microstructures of Fe20Cr25NiNb stainless steel oxidized at 1000°C for 4 h with different relative humidity values. Although the steel specimens are covered by the oxides after the corrosion testing, some parallel scratches can be observed on the steel surface for all conditions, indicating that the thickness of oxide film formed on the steel surface is too thin to completely cover the original scratches generated during the grinding process.[26] For the condition with 0% relative humidity, many small nodules with size of ~ 10 μm are formed on the oxide film, as shown in Fig. 2a. It also can be found that the thin oxide film has been subjected to the spallation, and some fresh steel regions are present on the matrix surface of Fe20Cr25NiNb stainless steel, as indicated by the white arrows in Fig. 2a. When the relative humidity reaches 20%, except the thin oxide film and small nodules, some large nodules with white-colored contrast in SEM micrograph are also generated, as shown in Fig. 2b. With the further increase of relative humidity, it can be seen from Fig. 2b and e that the number and size of these white-colored large nodules increase slightly. This is because the oxygen partial pressures in the high-temperature environment increase with the increase of relative humidity (presented in section "Effect of Relative Humidity on the Corrosion Behaviors"); more oxides can be formed under higher oxygen partial pressures.[27] The following will focus on the detail analysis of the small nodules and the white-colored large nodules.

Figure 3 shows the enlarged microstructure and EDS results of Fe20Cr25NiNb stainless steel oxidized at 1000°C for 4 h with 0% relative humidity. Figure 3b shows that some cracks are formed on the
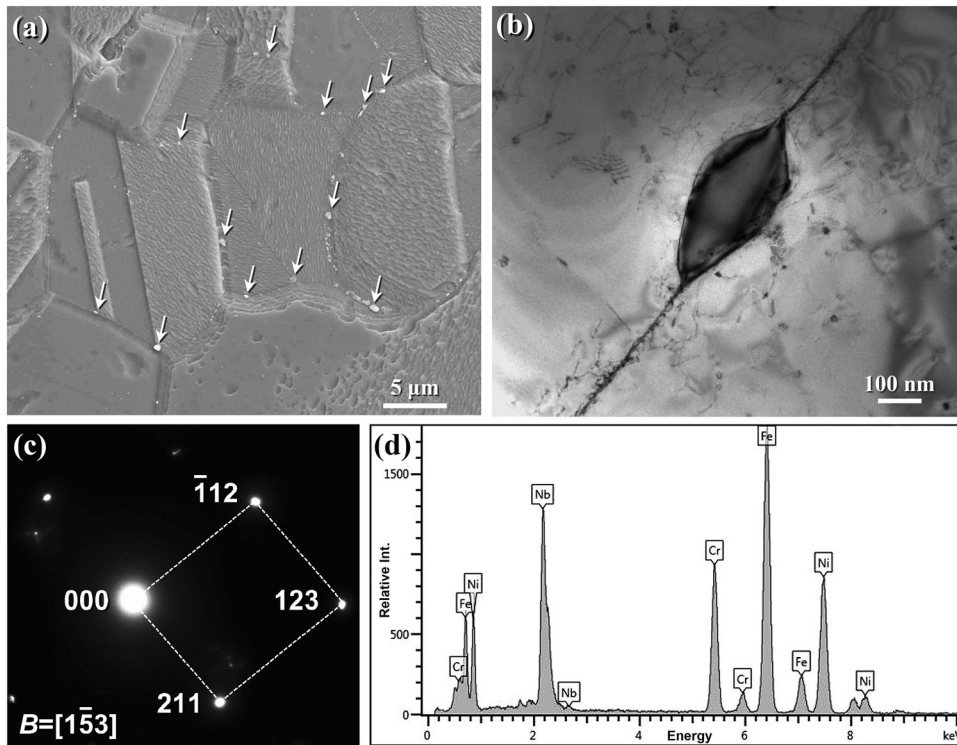
Fig. 1. Microstructures and phases of the un-oxidized Fe20Cr25NiNb stainless steel. (a) SEM micrograph; (b) TEM micrograph of the intergranular phases; (c) selected area electron diffraction pattern of the intergranular phases in (b); (d) EDS results of the intergranular phases in (b).

top of the small nodules. The formation of cracks is primarily attributed to the volume mismatch between the steel matrix and oxides during the oxide growth. It is well known that larger growth stresses can be developed at the oxide/matrix interface during the corrosion process, and the stresses are compressive state in the oxide layer and tensile state in the steel matrix.[28] Under the compressive stresses, the buckling of oxide layer may occur, resulting in the formation of small nodules and micro-cracks.[13] EDS results show that the chemical composition of small nodules (micro-zone 1 in Fig. 3b) is similar to the thin oxide film (micro-zone 3 in Fig. 3b), as presented in Table I. These small nodules and thin oxide film are rich in chromium and oxygen, and the atomic ratio of chromium and oxygen is approximately 2:3, indicating that these oxides are probably chromia (Cr_2O_3). Figure 4 presents the XRD patterns of the oxidized Fe20Cr25-NiNb stainless steels with 0% relative humidity; these XRD results verify that the small nodules and oxide film are primarily composed of Cr_2O_3. At the spallation regions, many white particles are observed in the steel matrix, as shown in Fig. 3c. The EDS results in Table I indicate that the Nb content in the region with white particles (micro-zone 2) is higher than the original matrix content. Considering the size of these white particles is too small, the EDS values are the mixture of white particles and underlying matrix. Therefore, it can be speculated that these white particles are rich in

Nb. Combined with the microstructural results of the un-oxidized Fe20Cr25NiNb stainless steel in Fig. 1, these white particles are comparable in size to Fe_2Nb Laves phases. Based on the chemical compositions and particle size results, it can be inferred that these white particles are Fe_2Nb Laves phases and/or their oxides.

Figure 5 shows the enlarged microstructure of the oxidized Fe20Cr25NiNb stainless steel with 20% relative humidity. These white-colored large nodules are primarily composed of many small oxide crystals, as shown in Fig. 5b. The EDS results (Table I) show that these oxide crystals (micro-zone 4 in Fig. 5a) are rich in iron and oxygen and their atomic ratio is approximately 3:4, combining with the XRD patterns shown in Fig. 4, so it can be concluded that these oxide crystals are mainly magnetite (Fe_3O_4). At the regions with thin oxide film, the spallation of chromia layer is also observed, as presented by the red arrows in Fig. 5a. This phenomenon indicates that the thin oxide film is always falling off during the corrosion process even after the large nodules are formed. In addition, some small nodules also can be found on the surface in the regions of thin oxide film, and the micro-cracks are also presented on the top of these small nodules, as shown in Fig. 5d. These results indicate that the micrograph and phases at the regions with thin oxide film are the same as the specimen oxidized with 0% relative humidity, except for the formation of white-colored large nodules.
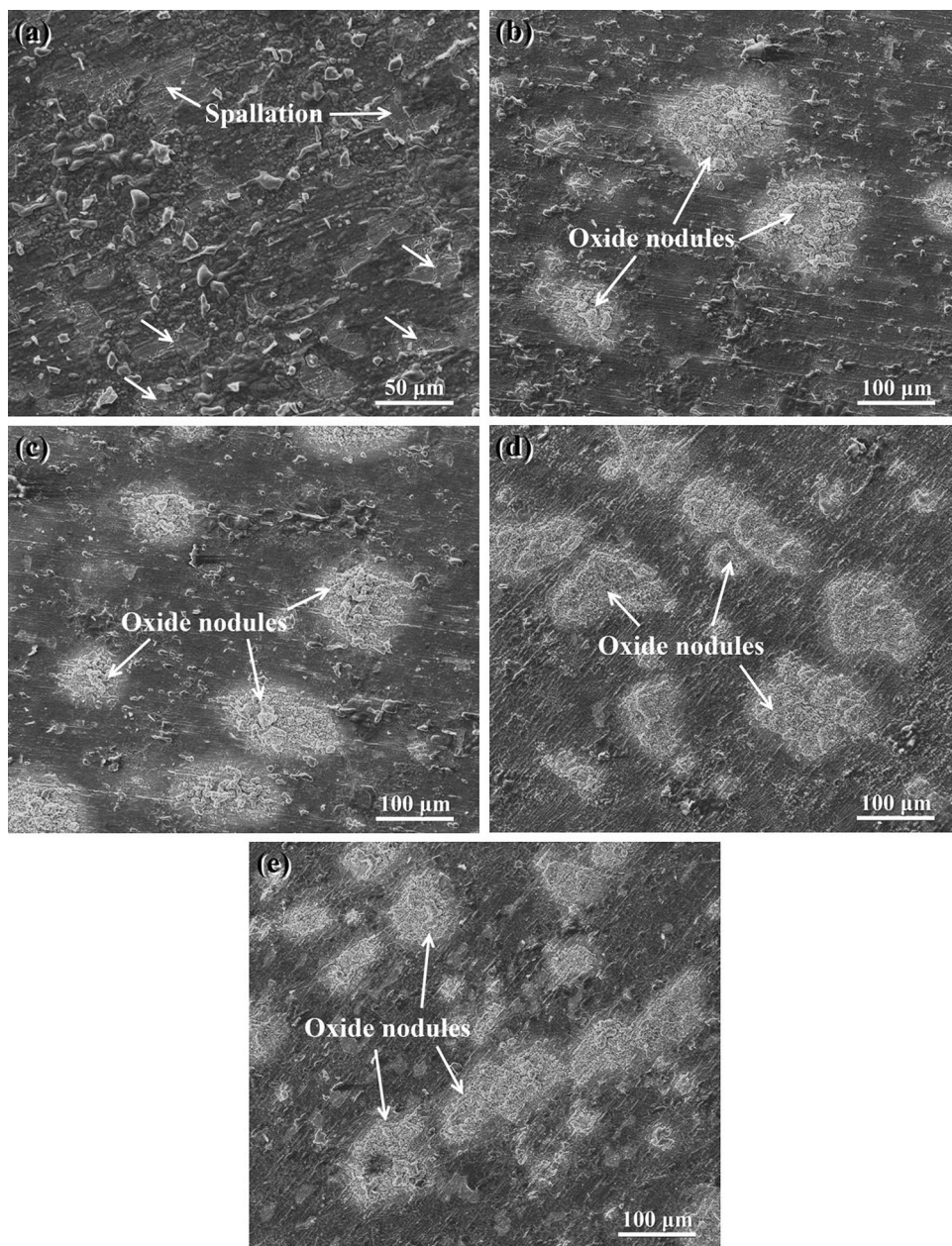
Fig. 2. Surface microstructures of Fe20Cr25NiNb stainless steel oxidized at 1000°C with different relative humidity values. (a) 0%; (b) 20%; (c) 40%; (d) 60%; (e) 80%.

As mentioned above, the corrosion products formed on the Fe20Cr25NiNb stainless steel include the thin oxide film, small nodules and white-colored large nodules. In the following, the cross-sectional microstructures of these corrosion products will be presented and analyzed. Figure 6 shows the cross-sectional microstructures of the regions with thin oxide film of the oxidized Fe20Cr25NiNb stainless steel with different relative humidity values. For all conditions, the thicknesses of oxide layer at the regions with thin oxide film are between 1 μm and 2 μm; there is no direct relationship between relative humidity and thickness of oxide layer, i.e., the relative humidity seems to have little effect on the thickness. In general, the higher the oxygen partial pressure, the more oxides will be formed on the alloy surface.[29] However, the thickness of the oxide film does not significantly increase with the increase of oxygen partial pressure (relative humidity) in the present study. This phenomenon can be explained by the reason that the oxygen partial pressure at lower relative humidity is sufficient for the formation of chromia, and the growth of chromia layer is mainly controlled by the diffusion of Cr cations and O anions through the oxide layer at higher temperatures.[30] Therefore, all the oxidized specimens have the similar thickness of oxide layer because of the same corrosion temperature and exposure time.
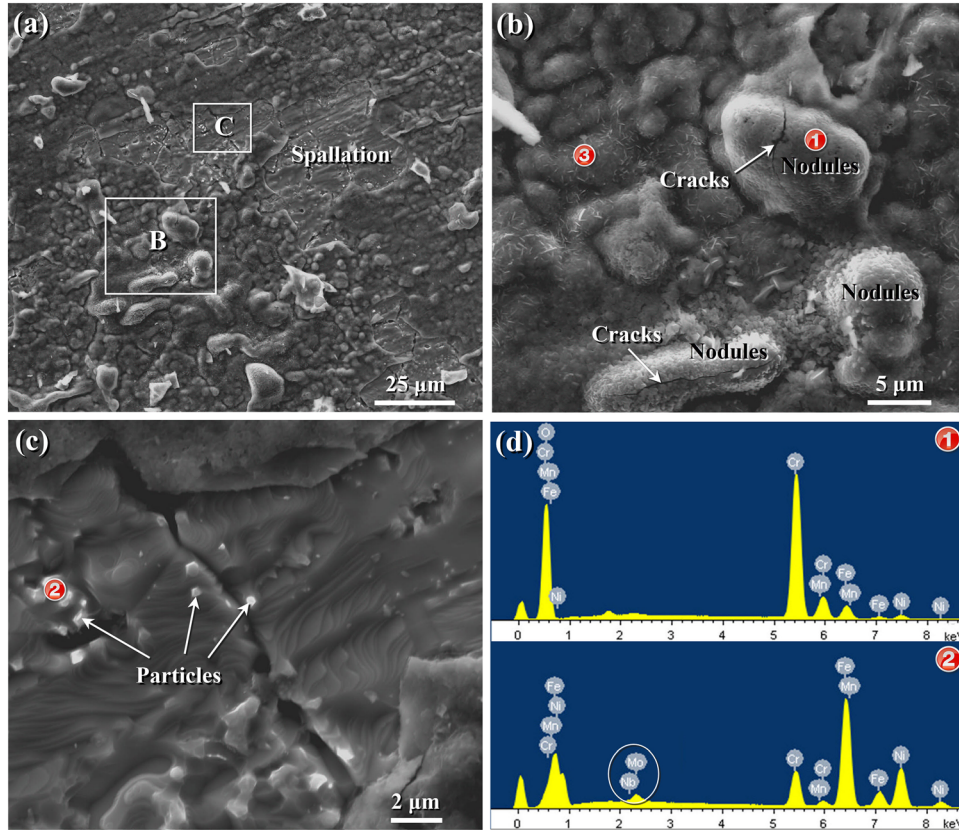
Fig. 3. Enlarged microstructure and EDS results of the oxidized Fe20Cr25NiNb stainless steel with 0% relative humidity. (a) SEM micrograph; (b) and (c) are the enlarged micrographs of the rectangular regions marked by "**B**" and "**C**" in (a), respectively; (d) EDS results of small nodules and white particles in (b) and (c) (Color figure online).

Table I. EDS results of chemical compositions (at.%) of the micro-zones marked by red numbers 1–5 in Figs. 3 and 5

Micro-zones	O	Cr	Fe	Ni	Mn	Mo	Nb	Possible phases
1	57.49	38.25	2.67	0.48	1.11	–	–	Cr_2O_3
2	–	13.74	55.16	27.74	0.29	1.32	1.75	Matrix
3	56.92	37.63	2.95	1.24	0.86	-	0.40	Cr_2O_3
4	51.86	3.42	40.55	3.31	0.37	–	0.49	Fe_3O_4
5	59.75	34.63	3.61	1.37	0.56	–	0.08	Cr_2O_3

Figure 7 shows the cross-sectional microstructure and corresponding EDS results of the regions with small nodules of the oxidized Fe20Cr25NiNb stainless steel with 20% relative humidity. It can be clearly seen that some new oxides are generated between the oxide film and the steel matrix, and these new-generated oxides are rich in chromium and oxygen, as shown in Fig. 7a. Obviously, it can be inferred that their chemical compositions are similar to the chromia layer, and these oxides are Cr_2O_3. In addition, an interesting thing is that some Nb-rich phases are located at both sides of the new formed oxides, as shown in the Nb mapping image of Fig. 7a and the Nb scanning line results of Fig. 7b. In fact, the Nb-rich phases are observed near almost every region with small nodules on the oxidized

Fe20Cr25NiNb stainless steel. This indicates that the formation of this new-generated Cr_2O_3 is strongly related to the Nb-rich phases. Considering the fact that many intergranular Fe_2Nb phases are distributed in the steel matrix (Figs. 1 and 3c), some Fe_2Nb Laves phases inevitably meet the matrix/oxide interface during the corrosion process and these Fe_2Nb Laves phases can transform into the niobium pentoxide (Nb_2O_5) by reaction with oxygen.[31] A large volumetric expansion will occur at the oxide interface under these regions with Fe_2Nb Laves phases because of the large Pilling–Bedworth ratio of Nb_2O_5 (~ 2.67),[32] which can result in the buckling of oxide film and the formation of micro-cracks. Furthermore, the micro-cracks can serve as rapid channels for the oxygen diffusion from the

Initial Corrosion Behaviors of Fe20Cr25NiNb Stainless Steel in High Temperature Environment with Different Relative Humidity Values
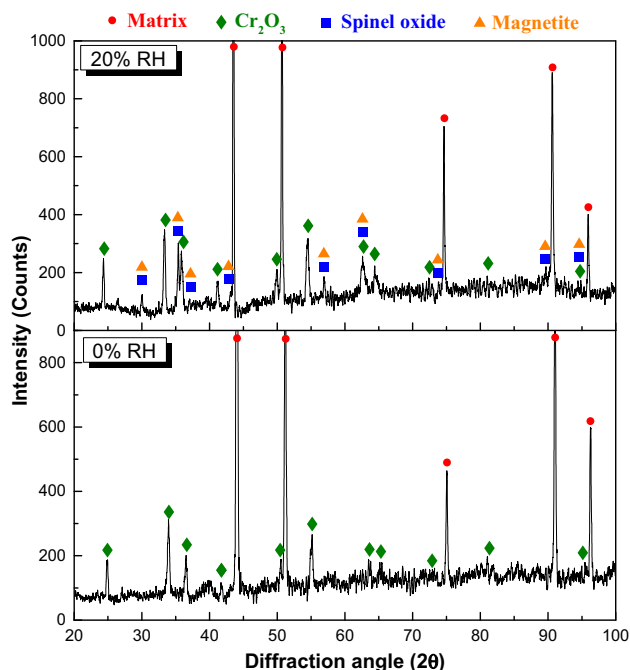
3927

Fig. 4. XRD patterns of the oxidized Fe20Cr25NiNb stainless steels with 0% relative humidity and 20% relative humidity.

outer environment into the oxide interface, promoting the formation of the new-generated Cr_2O_3.[13]

Figure 8 shows the cross-sectional microstructure and corresponding EDS results of the regions with white-colored large nodules of the oxidized Fe20Cr25NiNb stainless steel with 20% relative humidity. It can be found that the thickness of the oxide layer at the regions with large nodules (> 10 μm) is obviously larger than the thin oxide film (1–2 μm) and the small nodules. This oxide layer is primarily divided into three layers. The outer layer is composed of some oxide crystals and is rich in oxygen and iron, as shown in the Fe and O mapping images of Fig. 8a and the scanning line results of Fig. 8b. Combining with their morphology and chemical compositions, it can be inferred that these oxide crystals are Fe_3O_4, as same as the small oxide crystals in Fig. 5b. The inner layer has a darker color comparing with the outer layer, and the chemical compositions of the inner layer mainly consist of iron, oxygen, nickel and chromium, as shown in Fig. 8b. Usually, the duplex oxide layer with outer Fe_3O_4 layer and inner $(Fe, Cr, Ni)_3O_4$ spinel layer can be formed on the stainless steels at high temperatures after the pre-formed chromia film is subjected to spallation.[13,33] Consequently, this inner layer should be the $(Fe, Cr, Ni)_3O_4$ spinel oxides in the present study. In addition, a (Cr, O)-rich healing layer with thickness of about 2 μm can be observed near the steel matrix, and the (Cr, O)-rich healing layer should be mainly composed of Cr_2O_3. This healing layer is usually formed at the oxide/matrix interface by the inward diffusion of

oxygen from the outer environment and the outward diffusion of chromium from the steel matrix.[20]

Weight Gains of Fe20Cr25NiNb Stainless Steel During Corrosion Process

Figure 9 shows the weight gains of Fe20Cr25-NiNb stainless steel oxidized at 1000°C for 4 h with different relative humidity values. For all corrosion conditions, the weight gains of Fe20Cr25NiNb stainless steel progressively increase with the increase of exposure time, and the higher the relative humidity, the greater the weight gains, as shown in Fig. 9a. It also can be found that the transition point occurs in the weight gain curves for the conditions with ≥ 20% relative humidity. The transition times of Fe20Cr25NiNb stainless steel with 20% relative humidity, 40% relative humidity, 60% relative humidity and 80% relative humidity are ∼ 2.5 h, ∼ 1.64 h, ∼ 1.32 h and ∼ 1.27 h, respectively. In other words, the higher the relative humidity is, the shorter the transition time. After the transition point, the accelerated corrosion can be clearly observed from the weight gain curves, and the corrosion kinetics has changed before and after the transition point, as shown in Fig. 9. In general, the corrosion kinetics of steels at high temperatures can be calculated by the following Eq.:[13]

$$(\Delta W)^n = K \cdot t \qquad (1)$$

where ΔW is the weight gain per unit area (mg/cm^2), n is the power exponent for representing the corrosion kinetic, K is the corrosion rate constant (mg^n/cm^{2n}/h), and t is the exposure time.

By fitting the weight gain results with the above equation, the kinetic parameters can be obtained from the fitted curve. The fitted kinetic parameters of Fe20Cr25NiNb stainless steel oxidized at 1000°C before and after the transition point are summarized in Table II. Before the transition point, the power exponent n is between 1.16 and 1.45, and its value decreases generally with increase of relative humidity. After the transition point, the power exponent n increases to 1.56 for the condition with 20% relative humidity and reaches ∼ 2 for the conditions with higher relative humidity. In general, the corrosion kinetics of steels and alloys at high temperatures generally fall between two extreme cases: a linear law (n = 1) and a parabolic law (n = 2). For the linear law, the formation rate of oxide film is directly proportional to exposure time, and the corrosion reaction is so fast that the metal atoms will react with oxygen as long as the metal meets oxygen. For the parabolic law, the corrosion reaction is diffusion-controlled, and the reaction rate is equal to the diffusion rate of the reactants through the oxide layer.[34] Therefore, it can be inferred that the oxide growth of Fe20Cr25NiNb stainless steel primarily follows the linear law before the transition point in view of the smaller
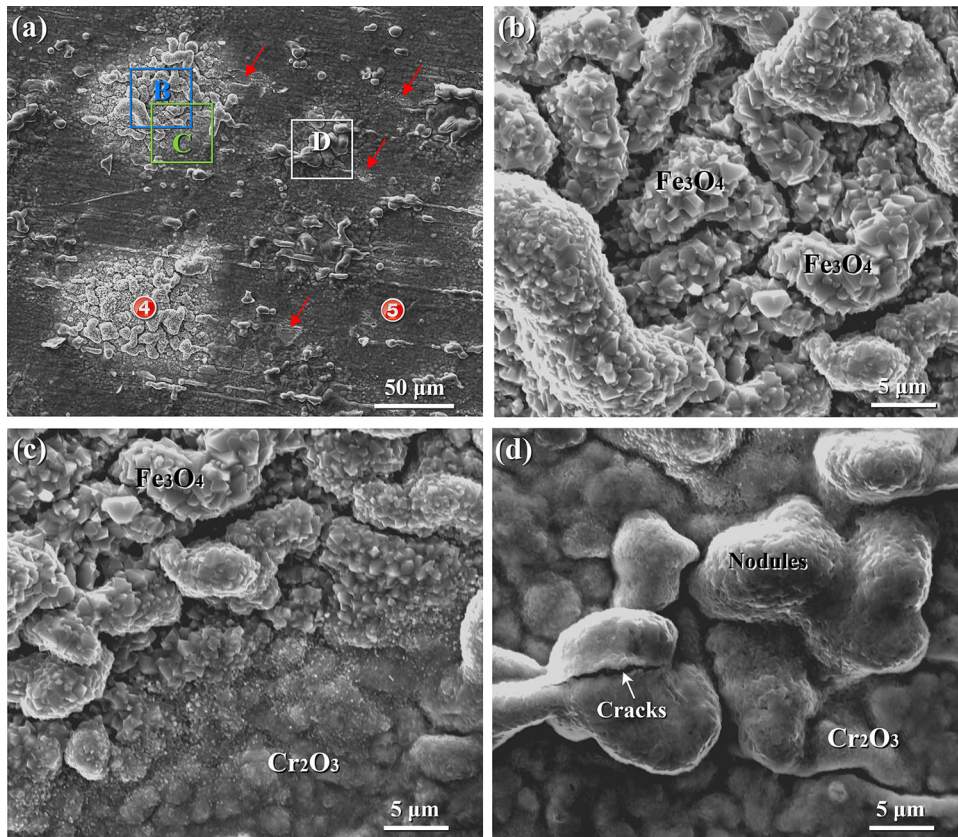
Fig. 5. Enlarged microstructure of the oxidized Fe20Cr25NiNb stainless steel with 20% relative humidity. (a) SEM micrograph; (b), (c) and (d) are the enlarged micrographs of the rectangular regions marked by "**B**", "**C**" and "**D**" in (a), respectively.

power exponent ($n < 1.5$). After the transition point, the oxide growth for the condition with 20% relative humidity may obey the mixture of linear law and parabolic law considering the intermediate power exponent ($n \approx 1.5$), and the corrosion growth for the conditions with higher relative humidity obeys the parabolic law ($n \approx 2$).

In addition, it can be found that the corrosion rate constant K increases generally with the increase of relative humidity when the corrosion primarily follows the linear law (before the transition point), and the similar phenomenon also can be observed when the corrosion obeys the parabolic law (after the transition point, relative humidity $\geq 40\%$), as presented in Table II. It is widely accepted that when the corrosion rate constant is larger for the similar corrosion condition, the corrosion of steels and alloys at high temperature is more severe.[35] This indicates that more corrosion products are generated on the steel surface at higher relative humidity because of the higher oxygen partial pressure in the oxidizing environment.

Effect of Relative Humidity on the Corrosion Behaviors

Combining the microstructural results with the weight gains of Fe20Cr25NiNb stainless steel

oxidized at 1000°C, it can be concluded that the accelerated corrosion after the transition point is attributed to the formation of white-colored large nodules, because the white-colored large nodules have been observed on the oxidized specimens with accelerated corrosion ($\geq 20\%$ relative humidity) while only thin oxide film and small nodules are formed on the specimens without accelerated corrosion (0% relative humidity), as shown in Figs. 2 and 9. As mentioned above, the regions with white-colored large nodules possess a thicker oxide layer ($> 10~\mu m$) compared with the thin oxide film (1–2 μm) and small nodules; this thick oxide layer provides an additional and significant weight gain of Fe20Cr25NiNb stainless steel, which is presented in the form of accelerated corrosion after the transition point on the weight gain curve. In general, the formation of these large oxide nodules is usually associated with the cracking and spallation of pre-formed chromia film when the chromia-forming stainless steels are oxidized at high temperatures.[13,36] In the present study, the spallation of pre-formed chromia film is observed on the regions with thin oxide film for all corrosion conditions, while the white-colored large nodules are not formed on the steel surface for the condition with 0% relative humidity. This indicates that the

Initial Corrosion Behaviors of Fe20Cr25NiNb Stainless Steel in High Temperature
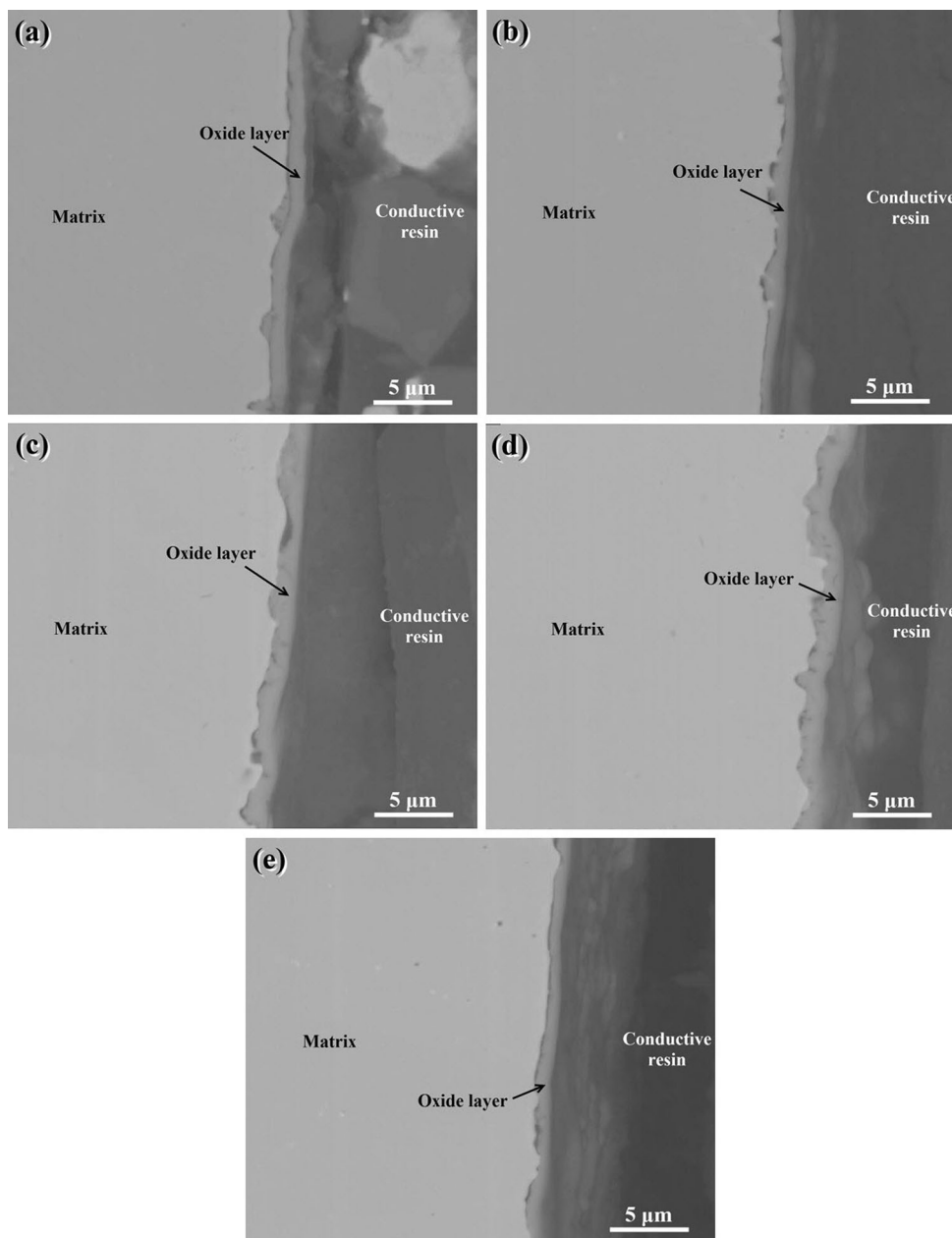Environment with Different Relative Humidity Values

3929

Fig. 6. Cross-sectional microstructures of the regions with thin oxide film of Fe20Cr25NiNb stainless steel oxidized at 1000°C with different relative humidity values. (a) 0%; (b) 20%; (c) 40%; (d) 60%; (e) 80%.

formation of white-colored large nodules is not only associated with the spallation of chromia film, but also has an important relationship with the relative humidity.

The relative humidity is closely related to the oxygen partial pressure, and the oxygen partial pressure directly determines the behaviors of many oxides.[37] In the present study, the content of water vapor was maintained at the target relative humidity at the temperature of 50°C in the steam generator before the helium gas was introduced into the reaction furnace. The pressure of the helium gas was always maintained at one atmosphere in the steam generator and reaction furnace during the entire corrosion process. Therefore, the oxygen partial pressure can be calculated based on the relative humidity values. The saturated water vapor pressure is about 1.218×10^{-1} atm at the temperature of 50°C according to the computation of Murray.[38] Therefore, the partial pressure of water vapor in the reaction furnace can be estimated in the present study, as presented in Table III. At higher temperatures, the water vapor will decompose into hydrogen and oxygen by the decomposition reaction $H_2O = H_2 + 1/2 O_2$, and the standard free energy change of this decomposition reaction is a function only of temperature, which is given by Eq. 2:[28]
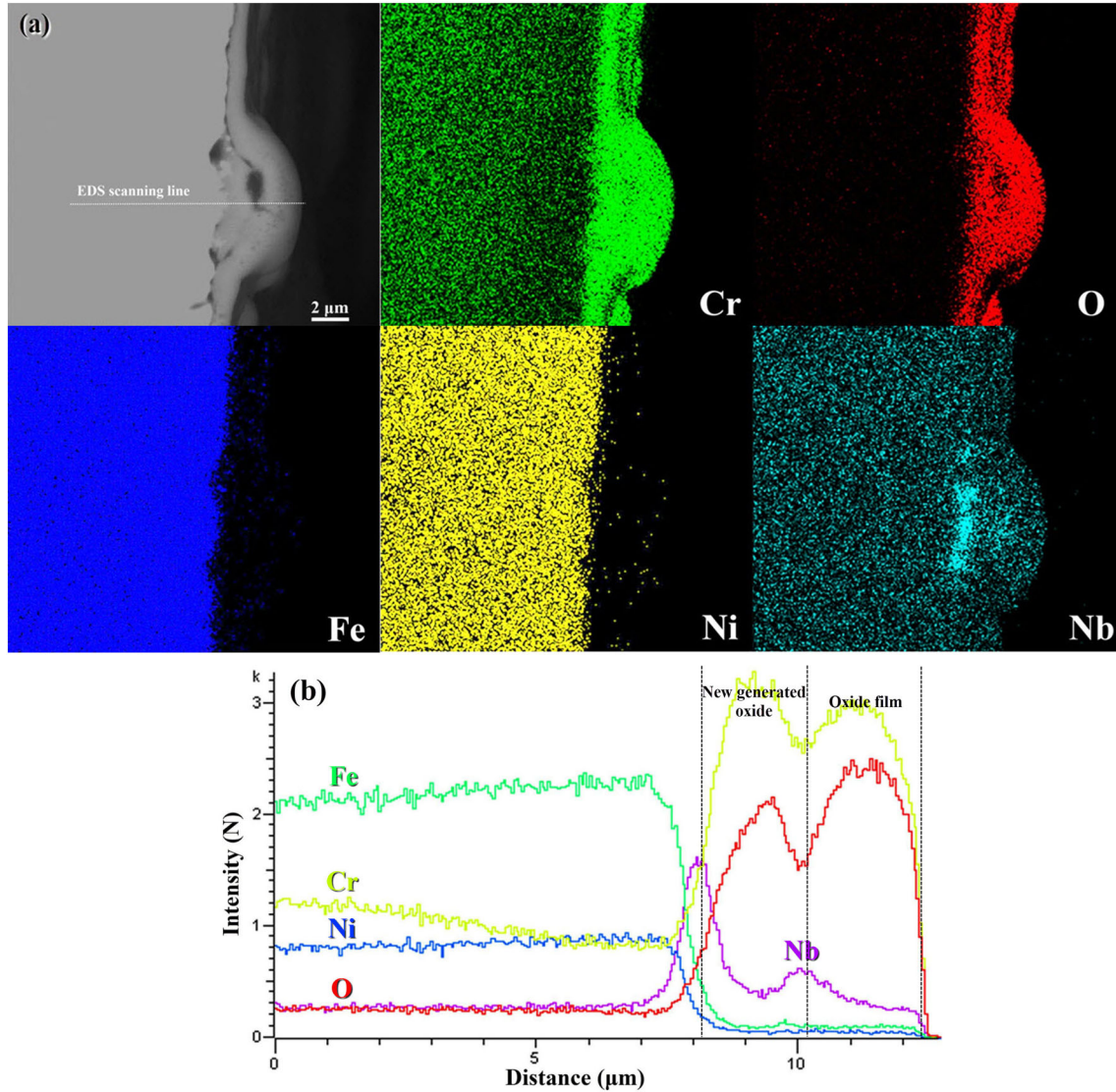
Fig. 7. Cross-sectional microstructure and corresponding EDS results of the regions with small nodules of the oxidized Fe20Cr25NiNb stainless steel with 20% relative humidity. (a) Cross-sectional microstructure and corresponding EDS mapping images; (b) EDS scanning line results.

$$\Delta G^{\circ} = 246440 - 54.8T \text{ J/mol} \quad (2)$$

where ΔG° is termed the standard free energy change. T is thermodynamic temperature. According to the thermodynamic relationship between metals and gases,[28] the equilibrium oxygen partial pressure can be calculated by Eq. 3:

$$K_p = \exp\left(-\frac{\Delta G^{\circ}}{RT}\right) = \frac{p_{H_2}p_{O_2}^{1/2}}{p_{H_2O}} \quad (3)$$

where K_p is the equilibrium constant at fixed total pressure, R is the gas constant, and p_{H_2O}, p_{O_2} and p_{H_2} are the partial pressure of water vapor, oxygen and hydrogen in the oxidizing environment, respectively. Considering that the helium gases with water vapor are constantly updated and only a small amount of water vapor is decomposed into

oxygen and hydrogen, it can be roughly estimated that the hydrogen partial pressure is twice the oxygen partial pressure and partial pressure of water vapor has not changed after the decomposition reaction in the furnace of thermal analyzer. Based on the above assumptions and equations, the oxygen partial pressure can be easily calculated in the present study, as presented in Table III.

In fact, the actual oxygen partial pressure for the condition with 0% relative humidity is higher than the calculated oxygen partial pressure (0 atm), because trace amounts of oxygen-containing impurities are inevitably present in the helium gases. It is well known that the equilibrium dissociation pressure of Cr_2O_3 at 1000°C is extremely low ($\sim 10^{-22}$ atm[39]), and the actual oxygen partial pressure for the condition with 0% relative humidity should be higher than the dissociation pressure of Cr_2O_3. Therefore, the chromia film and small nodules can be formed on
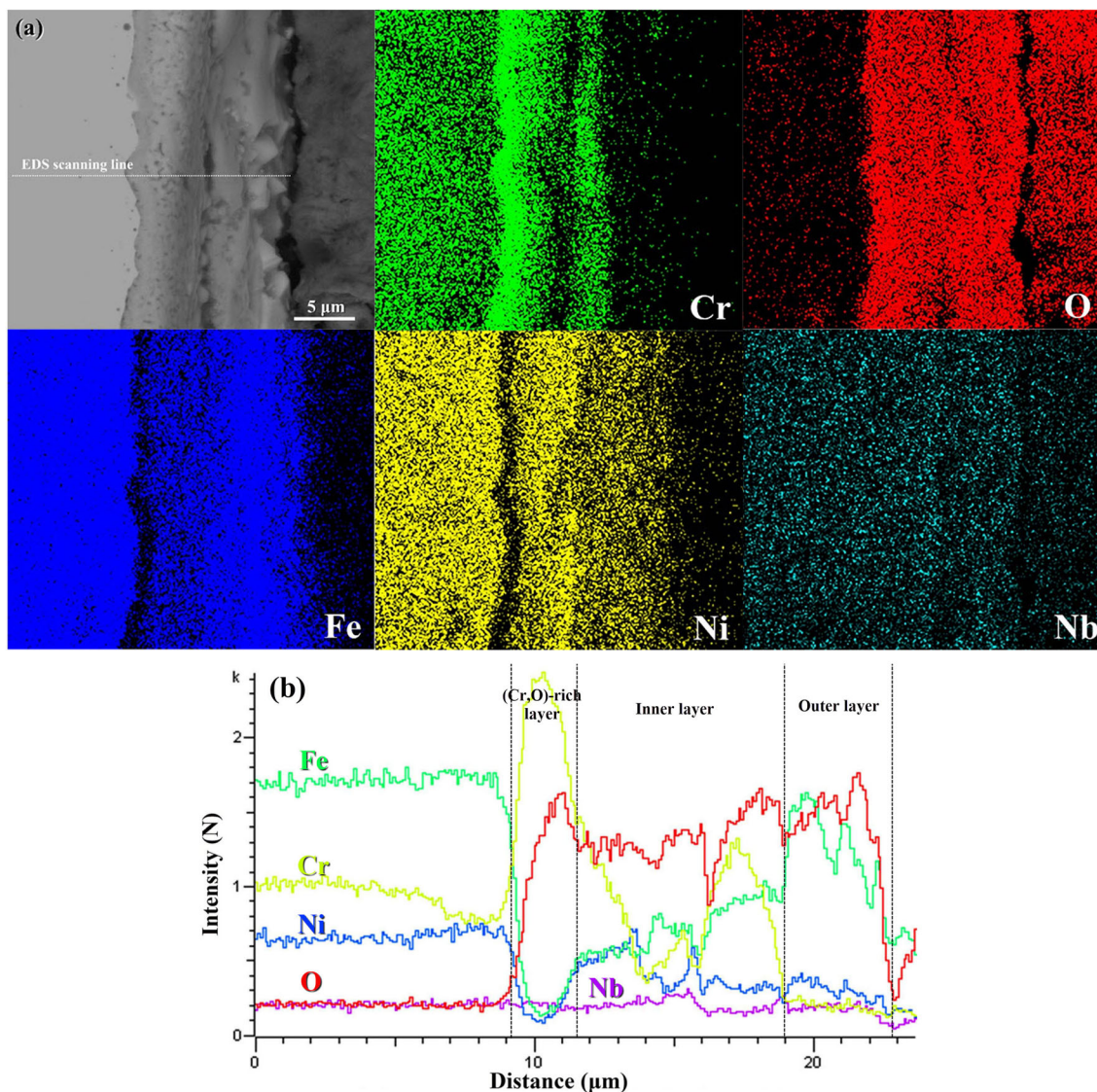
Fig. 8. Cross-sectional microstructure and corresponding EDS results of the regions with white-colored large nodules of the oxidized Fe20Cr25NiNb stainless steel with 20% relative humidity. (a) Cross-sectional microstructure and corresponding EDS mapping images; (b) EDS scanning line results.

the oxidized Fe20Cr25NiNb stainless steel. However, the equilibrium dissociation pressures of iron oxides at 1000°C increase significantly (2.8×10^{-12} atm for Fe_3O_4 and 1.7×10^{-6} atm for Fe_2O_3[30]), and it should be obviously larger than the actual oxygen partial pressure for the condition with 0% relative humidity; hence, the white-colored large nodules with iron oxides cannot be formed on the oxidized Fe20Cr25-NiNb stainless steel with 0% relative humidity even if the chromia film has been spalled. For the conditions with ≥ 20% relative humidity, the calculated oxygen partial pressure is around ~ 10^{-8} atm, which is several orders of magnitude higher than the dissociation pressure of Fe_3O_4 (2.8×10^{-13} atm[30]) and much lower than the dissociation pressure of Fe_2O_3 (1.7×10^{-6} atm[30]). Consequently, the Fe_3O_4 is successfully developed at the regions with white-

colored large nodules, and the Fe_2O_3 cannot not be observed certainly in the present system.

CONCLUSION

The initial corrosion behaviors of Fe20Cr25NiNb stainless steel were investigated in isothermal helium environment at 1000°C for 4 h, and the influence of relative humidity on the initial corrosion behaviors was discussed in the present study. Based on the experimental analysis and discussion, the following conclusions can be drawn:

(1) Thin chromia film and small nodules are formed on the oxidized steel surface for all corrosion conditions. For the conditions with ≥ 20% relative humidity, some white-colored large nodules are developed, and the number
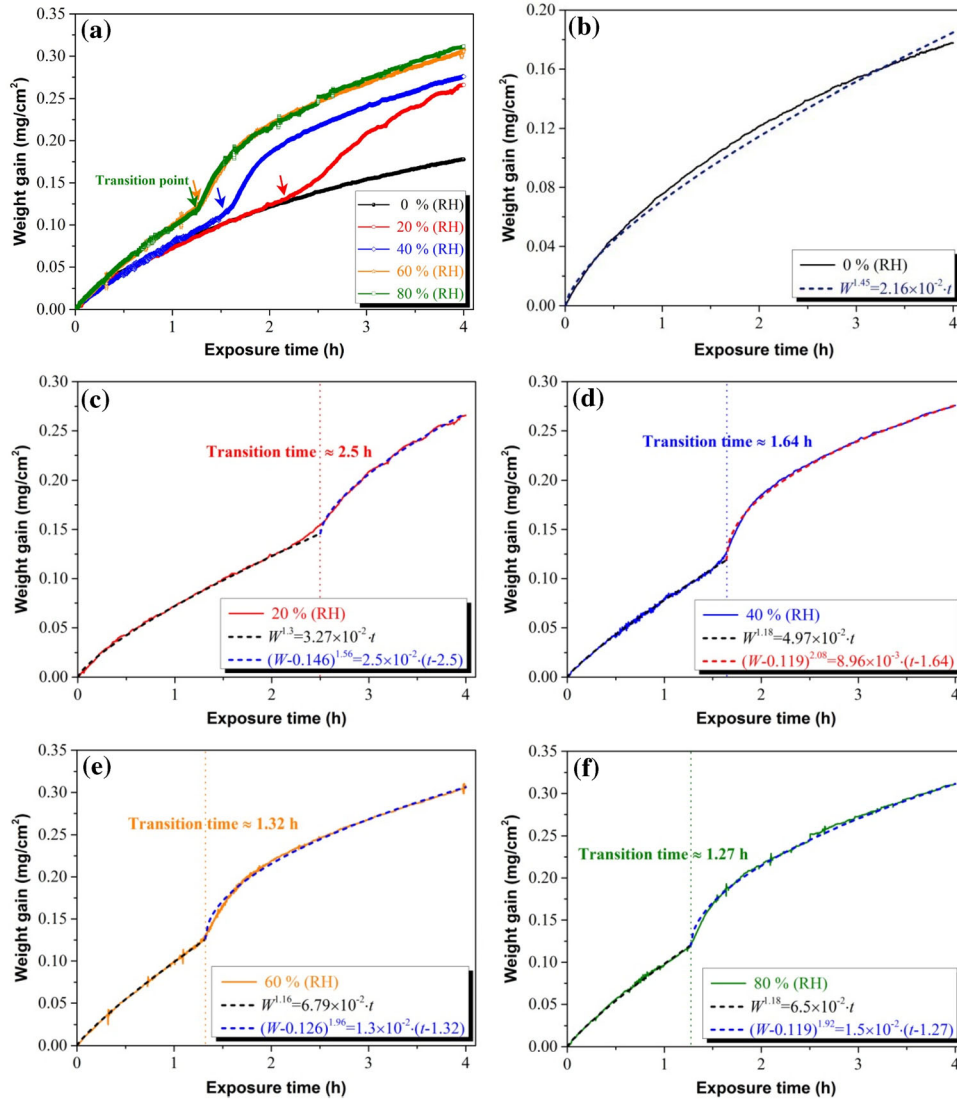
Fig. 9. Weight gains of Fe20Cr25NiNb stainless steel oxidized at 1000°C for 4 h with different relative humidity values. (a) Overall weight gains; (b) 0%; (c) 20%; (d) 40%; (e) 60%; (f) 80%.

Table II. The fitted kinetic parameters of Fe20Cr25NiNb stainless steel before and after the transition point

Relative humidity (%)	State	K (mg^n/cm^{2n}/s)	n
0	Before transition	2.16×10^{-2}	1.45
	After transition	−	−
20	Before transition	3.27×10^{-2}	1.3
	After transition	2.5×10^{-2}	1.56
40	Before transition	4.97×10^{-2}	1.18
	After transition	8.96×10^{-3}	2.08
60	Before transition	6.79×10^{-2}	1.16
	After transition	1.3×10^{-2}	1.96
80	Before transition	6.5×10^{-2}	1.18
	After transition	1.5×10^{-2}	1.92

Table III. The partial pressure of water vapor and calculated oxygen partial pressure for the oxidation conditions with different relative humidity values

Relative humidity (%)	Partial pressure of water vapor (kPa)	Oxygen partial pressure (atm)
0	0	0
20	2.468	1.693×10^{-8}
40	4.936	2.688×10^{-8}
60	7.404	3.522×10^{-8}
80	9.872	4.266×10^{-8}

and size of these large nodules increase slightly with the increase of relative humidity.

(2) The small nodules are primarily composed of the pre-formed chromia film and new-generated chromia phases, with some Nb-rich phases. The formation of small nodules is strongly related to the oxidation of intergranular Fe_2Nb phases. The white-colored large nodules mainly consist of three oxide layers: outer magnetite layer, inner spinel layer and (Cr,O)-rich healing layer at the oxide/matrix interface.

(3) The weight gains progressively increase with the increase of exposure time, and the higher the relative humidity, the greater the weight gains. For the conditions with $\geq 20\%$ relative humidity, an accelerated corrosion is clearly observed after the transition point and the accelerated corrosion is attributed to the formation of white-colored large nodules. The oxide growth primarily follows the linear law before the transition point and obeys the parabolic law after the transition point for higher relative humidity.

(4) The oxygen partial pressure directly determines the formation of oxides. For the condition with 0% relative humidity, the actual oxygen partial pressure should be higher than the dissociation pressure of chromia and lower than that of magnetite, resulting in the formation of chromia film and small nodules and the absence of white-colored large nodules. For the conditions with higher relative humidity, the large nodules with magnetite can be successfully developed because of the higher oxygen partial pressure.

ACKNOWLEDGEMENTS

CONFLICT OF INTEREST

On behalf of all authors, the corresponding author states that there is no conflict of interest.

SUPPLEMENTARY INFORMATION

The online version contains supplementary material available at https://doi.org/10.1007/s11837-022-05425-7.

REFERENCES

1. P.C. Rowlands, J.C.P. Garrett, L.A. Popple, A. Whittaker, and A. Hoaskey, *Nucl. Energy* 25, 267 (1986).
2. A. Shin, M. Chevalier, E. Laney, and J. Pearson, *Mater. High Temp.* 35, 30 (2018).
3. A. Rudge, *Mater. High Temp.* 22, 11 (2005).
4. R.N. Clark, Mapping of corrosion sites in advanced gas-cooled reactor fuel cladding in long term pond storage. Dissertation, Swansea University, (2018).
5. C. Degueldre, R.J. Wilbraham, J. Fahy, and S.M. Green, *J. Nucl. Mater.* 543, 152633 (2021).
6. C. Cabet and B. Duprey, *Nucl. Eng. Des.* 251, 139 (2012).
7. R.N. Clark, J. Searle, T.L. Martin, W.S. Walters, and G. Williams, *Corros. Sci.* 165, 108365 (2020).
8. IAEA, Review of Fuel Failures in Water Cooled Reactors, (IAEA Nuclear Energy Series No. NF-T-2.1, Vienna, 2010), pp. 1–2.
9. R.B. Rebak, W.P. Gassmann and K.A. Terrani, Managing nuclear power plant safety with FeCrAl alloy fuel cladding. Paper presented at Top Safe 2017, IAEA Safety in Reactor Operation, Vienna, Austria, 12–16 February (2017).
10. D.R. Olander, *Fundamental Aspects of Nuclear Reactor Fuel Elements* (Technical Information Center, Springfield, Virginia, 1976), pp 373–462.
11. E. Nonbol, Description of the Advanced Gas Cooled Type of Reactor (AGR), (Risø National Laboratory, Roskilde, Denmark, NKS/RAK-2(96)TR-C2, 1996), pp. 10–12.
12. D. Hambley, Technical basis for extending storage of the UK's advanced gas-cooled reactor fuel. Paper presented at Proceedings of GLOBAL 2013: International Nuclear Fuel Cycle Conference, Salt Lake City, UT, 29 Sep–3 Oct 2013.
13. H. Chen, H. Wang, Q. Sun, C. Long, T. Wei, S.H. Kim, and C. Jang, *Corros. Sci.* 145, 90 (2018).
14. J.W. Tyler, *Oxid. Met.* 24, 149 (1985).
15. P.K. Madden and V.M. Callen, *J. Nucl. Mater.* 113, 46 (1983).
16. C. Degueldre, J. Fahy, O. Kolosov, R.J. Wilbraham, M. Döbeli, N. Renevier, and S. Ritter, *J. Mater. Eng. Perform.* 27, 2081 (2018).

17. C. Barcellini, Microstructural Evolution of AGR Steel Cladding During Processing and Proton Irradiation. Dissertation, University of Manchester, (2019).
18. G.C. Allen, P.A. Tempest, J.W. Tyler, and R.K. Wild, *Oxid. Met.* 21, 187 (1984).
19. W.M. Pragnell and H.E. Evans, *Oxid. Met.* 66, 209 (2006).
20. R.C. Lobb and H.E. Evans, *Corros. Sci.* 24, 385 (1984).
21. H.E. Evans, *Mater. Sci. Tech.* 4, 414 (1988).
22. R.W. Swindeman, Development of a modified 310 stainless steel. Fossil Energy Program Annual Progress Report for April 1996 Through March 1997, Oak Ridge National Laboratory Report ORNL-6924, (1997).
23. C.S. Tedmon, D.A. Vermilyea, and J.H. Rosolowski, *J. Electrochem. Soc.* 118, 192 (1971).
24. B. Shassere, Y. Yamamoto, J. Poplawsky, W. Guo, and S.S. Babu, *Metall. Mater. Trans. A* 48, 4598 (2017).
25. N. Takata, H. Ghassemi-Armaki, M. Takeyama, and S. Kumar, *Intermetallics* 70, 7 (2016).
26. H. Chen, S.H. Kim, and C. Jang, *J. Mater. Sci.* 55, 3652 (2020).
27. H. Sakai, T. Tsuji, and K. Naito, *J. Nucl. Sci. Tech.* 21, 844 (1984).
28. D.J. Young, *High Temperature Oxidation and Corrosion of Metals* (Elsevier, Oxford, 2008), pp 315–356.
29. H. Yin, W.Y.D. Yuen, and D.J. Young, *Mater. Corros.* 63, 869 (2012).
30. T.P. Li, *High Temperature Oxidation and Hot Corrosion of Metals* (Chemical Industry Press, Beijing, 2003), pp 29–62.
31. C. Nico, T. Monteiro, and M.P.F. Graça, *Prog. Mater. Sci.* 80, 1 (2016).
32. T. Wei, J. Lin, C. Long, and H. Chen, *Acta Metall. Sin.* 52, 209 (2015).
33. H. Chen, S.H. Kim, C. Kim, J. Chen, and C. Jang, *Corros. Sci.* 156, 16 (2019).
34. A.S. Khanna, *High Temperature Corrosion* (World Scientific, Singapore, 2016), pp 1–32.
35. K. Zhao, S. Ouyang, Y. Liu, B. Liu, X. Liang, and Y. Wang, *Trans. Nonferrous Met. Soc. China* 29, 526 (2019).
36. J. Yuan, W. Wang, H. Zhang, L. Zhu, S. Zhu, and F. Wang, *Corros. Sci.* 109, 36 (2016).
37. S.R.J. Saunders, M. Monteiro, and F. Rizzo, *Prog. Mater. Sci.* 53, 775 (2008).
38. F.W. Murray, *J. Appl. Meteorol.* 6, 203 (1967).
39. M. Michalik, M. Hänsel, J. Zurek, L. Singheiser, and W.J. Quadakkers, *Mater. High Temp.* 22, 213 (2005).